Journal of Physics B: Atomic, Molecular and Optical Physics

PAPER

Control of high-harmonic generation from periodic asymmetric lattices

To cite this article: Tian-Jiao Shao *et al* 2023 *J. Phys. B: At. Mol. Opt. Phys.* **56** 165401

View the article online for updates and enhancements.

You may also like

- Future directions for active matter on ordered substrates
C. Reichhardt, A. Libál and C. J. O. Reichhardt
- Electron Transport through Magnetic Superlattices with Asymmetric Double-Barrier Units in Graphene
Qiu-Hong Huo, , Ru-Zhi Wang et al.
- Spontaneous polarization effects on solid high harmonic generation in ferroelectric lithium niobate crystals
Tian-Jiao Shao, Fang Hu and Hong-Bo Chen

This content was downloaded from IP address 210.32.178.20 on 31/07/2023 at 13:02

IOP Publishing Journal of Physics B: Atomic, Molecular and Optical Physics
J. Phys. B: At. Mol. Opt. Phys. **56** (2023) 165401 (10pp) https://doi.org/10.1088/1361-6455/ace507

Control of high-harmonic generation from periodic asymmetric lattices

Tian-Jiao Shao[1,2,*], Qiu-Lan Zhang[1], Ya-Dong Song[2,3,*] and Huan-Qing Zou[1]

[1] School of Information Science and Engineering, NingboTech University, Ningbo 315100, People's Republic of China
[2] State Key Laboratory of Magnetic Resonance and Atomic and Molecular Physics, Wuhan Institute of Physics and Mathematics, Innovation Academy for Precision Measurement Science and Technology, Chinese Academy of Sciences, Wuhan 430071, People's Republic of China
[3] School of Mathematics, Physics, and Information Science, Zhejiang Ocean University, Zhoushan, Zhejiang 316022, People's Republic of China

E-mail: shaotj@nit.zju.edu.cn and yadong_s@163.com

Received 19 March 2023, revised 1 July 2023
Accepted for publication 6 July 2023
Published 31 July 2023

Abstract

Periodic asymmetric lattices, viewed from one side to the other, have different spatial potential energies. This difference affects the electronic structure of valence electrons. Our work shows that pronounced even harmonic signals are observed from periodic asymmetric lattices driven by a multi-cycle pulse field. The phases of the odd and even harmonics driven by parallel and anti-parallel laser polarization directions are compared and show different dependences on laser polarization direction. Moreover, it is found that each burst in the synthesized attosecond pulse trains in a periodic asymmetric lattice shows the same carrier-envelope phase. We also show that the even-order harmonic efficiency in periodic asymmetric lattices can be enhanced (reduced) by using a multi-cycle driving laser in the presence of a weak terahertz pulse field.

Keywords: solid high-harmonic generation, periodic asymmetric lattice, permanent dipole moment, terahertz field

(Some figures may appear in colour only in the online journal)

1. Introduction

With the progress in the intense mid-infrared laser technology [1, 2], high-order harmonic generation (HHG) [3–14] from solids becomes an active topic for promising to synthesize extreme ultraviolet ultrashort laser sources with high brightness. Besides this, HHG from solids can be used to characterize the atomic or crystal structure [9, 12] with a sub-nanometer spatial scale, retrieve the electronic band structure [3], reconstruct the transition dipole moments of solids [15–17], probe the electron dynamics on the attosecond timescale, and so forth. High-harmonic generation from solids is generally understood by a three-step model [18–21]: the first step is the excitation of the valence band electrons through tunneling through the barrier formed by the periodic lattice potential and the strong laser field. In the second step, the excited electrons and holes are accelerated along the bands by the laser field. In the third step, since the laser field changes direction in each half cycle, the electrons will be driven back to recombine with the holes in the valence band, and harmonic photons are emitted. Besides the interband transition, the intraband current caused by the Bloch oscillations of the carrier along the band driven by the laser field also contributes to the total HHG emission. The excited electrons and the phase of the emitted harmonic photons record information on excitation, acceleration, and electron–hole recombination during the half-optical cycle HHG process.

The symmetry is important, which is the origin of the selection rule in the HHG of either gas [22] or solid [23–26]. In the gas phase, HHG with only odd harmonics will appear if the

* Authors to whom any correspondence should be addressed.

 © 2023 IOP Publishing Ltd

system possesses inversion symmetry. Both even and odd harmonics are generated if the medium does not have inversion symmetry [27–31].

The reason is that, for an asymmetric target like asymmetric diatomic molecules, the electrons are preferentially located in a deeper potential well in the driving field dressed Coulomb potential [27]. The laser field changes sign in the consecutive half-optical cycle, which causes differences in the laser-dressed barrier and leads to differences between the excitation rates in the consecutive half-optical cycles. This leads to the temporal HHG profile changing its minimum period from half optical cycle to one optical cycle, which results in the emergence of even harmonics in the frequency-domain spectra.

In this work, we investigate the control of HHG of periodic asymmetric potential by using the time-dependent Schrödinger equation (TDSE) [32–37] and semi-conductor Bloch equation (SBE) [18, 19, 38, 39]. We find that even harmonics appear in both the first and second plateaus of the HHG spectrum driven by a multi-cycle laser. For periodic asymmetric lattices, the phase of odd harmonics shifts π rad when the laser field is reversed; however, the phases of the even harmonics are independent of the reverse of the laser polarization.

Moreover, the synthesis of the attosecond pulse train on the basis of HHG in periodic asymmetric lattices is investigated. In each optical cycle of the driving field, one strong harmonic burst is generated in an earlier optical cycle, and a weak harmonic burst is generated in the following half-optical cycle driven by a multi-cycle field. The weak harmonic burst is ignored due to its low yield. Then, the two adjacent strong harmonic bursts have a time interval of one optical cycle of the driving field. This causes the two adjacent attosecond bursts to have the same carrier-envelope phase (CEP) and temporal profile. We also investigate the HHG from solids in the periodic asymmetric potential driven by a multi-cycle laser in the presence of a terahertz (THz) field, and the yield of even harmonics and phases of harmonics is found to be modulated by the relative strength ratio k_{THz} of the THz field.

2. Theoretical details

2.1. Groundstate

In the field-free case, the Schrödinger equations are given by [36],

$$\mathrm{i}\frac{\partial}{\partial t}\phi_\lambda^k(x) = \left[-\frac{\hbar^2}{2m_0}\nabla^2 + V(x)\right]\phi_\lambda^k(x). \tag{1}$$

where e and m_0 are the charges and the mass of the electron, respectively. $\phi_\lambda^k(x)$ is the field-free electron state initially located in λth band with initial crystal momentum k. $V(x)$ is the periodic Mathieu-type potential used in this work. By solving the above single-electron Schrödinger equation, the eigenstate and eigenvalue can be obtained. The periodic symmetric potential can be expressed as follows [37],

$$V_{\mathrm{s}}(x) = -V_0\left[1+\cos\left(2\pi x/a_0\right)\right]. \tag{2}$$

where $V_0 = 0.5603$ a.u., and $a_0 = 8$ a.u. is the lattice constant. The periodic asymmetric potential $V_{\mathrm{a}}(x)$ can be expressed as follows [37],

$$V_{\mathrm{a}}(x) = -V_0\left[2.5-\alpha\cos\left(4\pi x/a_0\right)-\beta\cos\left(2\pi x/a_0-\phi_r\right)\right]. \tag{3}$$

where $\alpha = 1.5$ and $\beta = 1.0$ are the unitless ratios describing the depth of the two wells inside the lattice. $\phi_r = \pi/2$ is the spatial phase term between the two frequency components. The parameters of the periodic potential are chosen in order to ensure the periodic symmetric potential V_{s}(x) and asymmetric potential V_{a}(x) have the same minimum energy band gap of 7.56 eV between the valence band maximum and conduction band minimum. The above type of asymmetric potential used in our work was first applied to investigate the interference induced by the recollision between the excited electrons with different nuclei sites in periodic solids in real-space [37].

According to Bloch's theorem, the Bloch function $\phi_\lambda^k(x)$ is expressed by a Bloch state,

$$\phi_\lambda^k(x) = \mathrm{e}^{\mathrm{i}kx}u_\lambda^k(x). \tag{4}$$

The Bloch state $u_\lambda^k(x)$ is a periodic function,

$$u_\lambda^k(x+a_0) = u_\lambda^k(x). \tag{5}$$

The Bloch state can be expanded by a group of $N_{\max}$ plane wave basis,

$$u_\lambda^k(x) = \sum_{j=1}^{N_{max}} C_{i,j}^k \exp[iK_j\cdot x], \tag{6}$$

where K_j is the reciprocal lattice vector, and the periodical potential $V(x)$ can be expanded by Fourier series as follows,

$$V(x) = \sum_{j=1}^{N_{\max}} V_j \exp\left[\mathrm{i}K_j\cdot x\right], \tag{7}$$

where V_j is,

$$V_j = \frac{1}{V_0}\int_{V_0} \mathrm{e}^{-\mathrm{i}K_j\cdot x}V(x)\mathrm{d}x, \tag{8}$$

where V_0 is the volume of the lattice. Then $u_\lambda^k(x)$ is inserted into field-free Schrödinger equations,

$$\sum_{j=1}^{N_{\max}}\left(\frac{\hbar^2}{2m_0}\left(k+k_j\right)^2\delta_{ij} + V_{k_i-k_j}\right)C_\lambda^{k,j} = \epsilon_\lambda^k C_\lambda^{k,i}. \tag{9}$$

By solving the above equation, the eigenvalue ϵ_λ^k and the expansion coefficient $C_{i,j}^k$ can be obtained. Then, the Bloch state $u_\lambda^k(x)$ and groundstate wavefunction $\phi_\lambda^k(x)$ can be obtained.

2.2. Time-dependent Schrödinger equations

In this work, the laser–crystal interaction is described by numerically solving the TDSE under the velocity gauge [33–37]. $\psi_\lambda^k(x,t)$ is the electron state initially located in λth band with initial crystal momentum k. The TDSE under the velocity gauge can be expressed as follows,

$$\mathrm{i}\frac{\partial}{\partial t}\psi_\lambda^k(x,t) = \left\{\frac{[\hat{p}+A(x,t)]^2}{2} + V(x)\right\}\psi_\lambda^k(x,t). \tag{10}$$

where $A(x,t)$ is the vector potential of the laser field.

In this work, since the wavelength of the driving laser is much larger than the lattice constant, the dependence of the driving field on spatial coordinates can be ignored. Thus, the dipole approximation is used, and the term of electron–light interaction $p\cdot A(x,t)$ is written as $p\cdot A(t)$. In addition, the higher-order term A^2 is much smaller than the other term in the above equation and is neglected. Then, equation (10) can be expressed as follows,

$$\mathrm{i}\frac{\partial}{\partial t}\psi_\lambda^k(x,t) = \left[-\frac{\hbar^2}{2m_0}\nabla^2 + p\cdot A(t) + V(x)\right]\psi_\lambda^k(x,t). \tag{11}$$

The time-dependent wavefunction $\psi_\lambda^k(t)$ can be expanded by the field-free eigenstate $\phi_\lambda^k(x)$,

$$\psi_\lambda^k(x,t) = \sum_\lambda \alpha_\lambda^k(t)\phi_\lambda^k(x), \tag{12}$$

where $\alpha_\lambda^k(t)$ is the expansion coefficient. Then the time-dependent Schrödinger equations in equation (11) can be expressed by,

$$\mathrm{i}\hbar\frac{\partial\alpha_q^k(t)}{\partial t} = E_q^k\alpha_p^k + \frac{e}{m_0}A(t)\sum_{l=1}^{N\max} p_{ql}^k\alpha_l^k(t). \tag{13}$$

where p_{ql}^k is transition dipole moment,

$$p_{ql}^k = \left\langle\phi_q^k|\hat{p}|\phi_l^k\right\rangle = \hbar\sum_{j=1}^{N\max}(k+k_j)\left(C_q^{k,j}\right)^* C_l^{k,j}. \tag{14}$$

Equation (13) can be solved by the Crank–Nicolson method,

$$\alpha_\lambda^k(t+\Delta t) = \frac{1-\mathrm{i}H\left(t+\frac{\Delta t}{2}\right)\frac{\Delta t}{2}}{1+\mathrm{i}H\left(t+\frac{\Delta t}{2}\right)\frac{\Delta t}{2}}\alpha_\lambda^k(t). \tag{15}$$

In the beginning, all of the electrons are located at the top valence band and all conduction bands are empty, then,

$$\alpha_q^k(t_{\text{initial}}) = \delta_{qn}. \tag{16}$$

After the expansion coefficient α_q^k is obtained, the time-dependent wavefunction $\psi^k(t)$ is obtained. The current at crystal momentum k is given by,

$$j_\lambda^k(t) = \frac{e}{m_0}\left(\left\langle\psi_\lambda^k(t)|p|\psi_\lambda^k(t)\right\rangle - eA(t)\right). \tag{17}$$

The total laser-induced current $j(t)$ is given by,

$$j(t) = \sum_\lambda\int j_\lambda^k(t)\mathrm{d}^3k. \tag{18}$$

By performing the Fourier transform of the laser-induced current $j(t)$, the HHG spectra are obtained.

2.3. Quasi-classical model

The driving field $E(t)$ used in our work is given by $E(t) = E_0 f(t)\cos(\omega_0 t)$, where E_0 is the amplitude of the driving field, $f(t)$ is the function of the envelope, ω_0 is the center frequency of the laser field, and the optical period $T_0 = 2\pi/\omega_0$. The vector potential $A(t)$ of the driving field is given by, $A(t) = -\int_{-\infty}^{t} E(t')\,\mathrm{d}t'$.

Since the laser-induced tunneling excitation rate has an exponential dependence on the bandgap, the electrons are supposed to be initially located at the Γ point in k space, which is the eigenstate on the top of the valence band. The motion of electrons in the k space can be expressed by [20],

$$k(t) = k_0 + \frac{e}{\hbar}A(t), \tag{19}$$

where k_0 is the initial wavevector at Γ point and $A(t)$ is the vector potential of the driving laser field. After excitation through tunneling, the electrons/holes perform Bloch oscillations driven by the laser field. When the electrons and holes recombine, a harmonic photon with energy equal to the difference of band energy at crystal momentum k is emitted,

$$\eta(t) = \frac{\varepsilon_\mathrm{c}(k(t)) - \varepsilon_\mathrm{v}(k(t))}{\hbar\omega_0}, \tag{20}$$

where $\varepsilon_\mathrm{c}(k(t))$ is the energy of electrons in the conduction band and $\varepsilon_\mathrm{v}(k(t))$ is the energy of holes in the valence band.

3. Results and discussion

3.1. Phases of the odd and even harmonics in periodic asymmetric potentials

Knowledge of the HHG phase allows for the evaluation of the highest occupied molecular orbital (HOMO) [40] and tomography of valence electrons of crystal [12]. In our work, we investigate the phases of the odd and even harmonics in a periodic asymmetric potential driven by a multi-cycle pulse.

In figure 1, the HHG spectra from both periodic symmetric potential and periodic asymmetric potential are driven by a 24-cycle trapezoidal laser pulse. The driving field has a total duration of 24 optical cycles (o.c.) and 2 o.c. ramp-up in our work. Therefore, except for the leading and tailing edge, from $T = -10T_0$ to $+10T_0$, the amplitudes of each cycle are the same. The amplitude of the multi-cycle driving pulse $E_0 = 0.011$ a.u. and wavelength $\lambda = 1600$ nm. In this work, the amplitude of $E_0 = 0.011$ a.u. corresponds to 98% of the boundary of the Brillouin zone ($k_{\max} = \pi/a_0 = 0.3927$ a.u.).

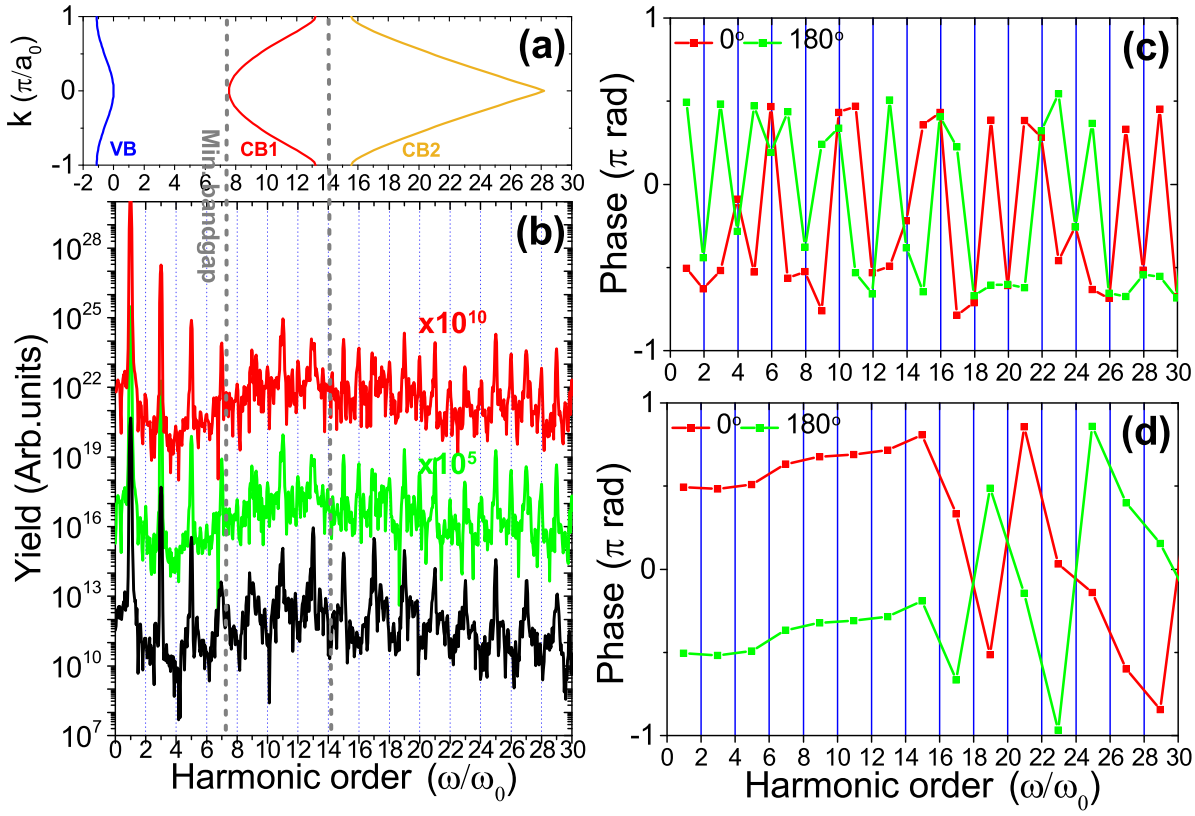

Figure 1. Polarization of driving laser field effects on the phase of the HHG spectra from a periodic asymmetric potential. (a) The band structure of the periodic asymmetric lattice calculated by using the Bloch states expansion method. (b) HHG spectra are driven by a multi-cycle laser field from the periodic symmetric potentials (black solid line), and the spectra are driven by the same multi-cycle field from asymmetric potentials with parallel (red solid line) and anti-parallel (green solid line) laser polarization directions. The gray dashed lines in figure 1(b) denote the minimum bandgap between CB1 and VB, and the bandgap energy between CB1 and VB at the boundary of BZ, which lead to the cutoff energy of the first plateau. (c) The phase of HHG spectra from periodic asymmetric potentials driven by parallel (red solid line) and anti-parallel (green solid line) laser polarization directions. (d) The phase of HHG spectra from periodic symmetric potentials driven by parallel (red solid line) and anti-parallel (green solid line) laser polarization directions. Simulated laser parameters: a field strength $E_0 = 0.011$ a.u., 24-cycle trapezoidal, 1600 nm laser field with 2 o.c. ramp-up.

Firstly, the relative direction of the peak of the multi-cycle laser relative to the permanent dipole is investigated. Figure 2 shows the field-free potential of the lattice (black solid line) and the direction of the permanent dipole, which is marked by the black arrows. The condition of parallel or (anti-)parallel is defined by the direction of the peak of the laser with respect to the permanent dipole. The red dashed line plots the field-dressed spatial potential of $V(x) + E_0 x$.

Figure 1(b) shows the calculated HHG spectra from a periodic asymmetric potential driven by 24 o.c. trapezoidal laser pulse with the parallel and anti-parallel laser polarization directions. The HHG spectra for a periodic symmetric potential driven by the same laser field are plotted using a black solid curve for comparison. In figure 1(b), for a periodic asymmetric potential, in addition to the sharp odd harmonics, pronounced even harmonics are observed both for the region of the first plateau and second plateau.

Besides the odd and even harmonic signals, some small peaks can be found in the HHG spectra in figure 1(b). This is because the system solved in TDSE is not a pure two-band system. In addition to the valence band, ten conduction bands are included in both the symmetric and asymmetric systems. The interband transitions between the different couples of energy bands interfere with each other, giving rise to the noise observed in HHG spectra. In the second, the dephasing effect is not considered in TDSE, and the dephasing time T_2 is considered to be infinitely large in TDSE simulations. Therefore, in addition to the long and short trajectories, multiple returns with excursion times larger than the long trajectories exist and interfere with each other, which cause the spectra to lose the clear frequency-comb structure.

The results shown in figures 1(a) and (b) can be explained by the laser-dressed spatial potential in figures 2(a) and (c). Because of the double-well structure of each lattice, the laser field dressed barrier is not inversely symmetric for the consecutive half cycle of the driving field. The electrons tend to locate in the deeper well. As shown in figure 2(d), when the laser field is parallel with the permanent dipole, the electron

energy is reduced due to the downshifting action of the laser field. This leads to a decrease in the tunneling excitation rate. In contrast, for the adjacent half cycle, the laser field is anti-parallel, and the electron energy is enhanced due to the upshifting action of the laser field, leading to an increase in the tunneling excitation rate. The differences between the tunneling excitation cause different harmonic photon yields of two consecutive half cycles. As shown in figures 2(b) and (d), in both the frequency range of the first plateau and second plateau, the temporal profile of HHG shows a minimum period in one optical cycle, which results in the emergence of even harmonics.

Figure 1(c) shows the phase of harmonic photons from a periodic asymmetric potential driven by a 24-cycle trapezoidal laser pulse with parallel (red solid line) and anti-parallel orientation (green solid line). For even harmonics, when the laser polarization becomes opposite, the phase of harmonics has nearly zero shift. The phases of the odd harmonics change by π rad. For comparison, for a periodic symmetric potential, when the 24-cycle trapezoidal laser pulse changes direction, the phase of the odd harmonics shifts by π rad as shown in figure 1(d).

Driven by a multi-cycle pulse, the reversal of the direction of the electric field is equivalent to the half-period phase shift of a multi-cycle pulse. This causes the phases of the odd harmonics to change by π rad, while the phases of the even harmonics will remain unchanged, independent of the system. A detailed discussion can be found in appendix B.

It is noted that the zero or π rad phase shifts caused by the reversal of the laser field are not exactly satisfied in figure 1(c) for low-order harmonics. This is because the harmonic photons in the frequency range of the plateau are emitted near the peak of the laser pulse, where the amplitude of the adjacent half-cycles is the same. For low-order harmonics, they are also contributed to by the trajectories from the leading and trailing edges of the laser. Since the laser cycles in the leading and trailing edges do not have the same amplitude, thus the phase shifts discussed above are not exactly satisfied for low-order harmonics.

In figures 3(a) and (b), a color plot of the evolution of the induced spatial electron density of the topmost valence band state $\psi^{\mathbf{k}=0}_{\lambda=VB}(x,t)$ inside the lattice is shown. The red (blue) color shows the place where the electron density of the valence band is high (low). The electron density plot shows the oscillations of the dipole moment in the time domain, which is responsible for the HHG emission.

For the periodic symmetric lattice in figure 3(a), the dipole moment oscillated in a minimum period of half the optical cycle of the driving field, while for the periodic asymmetric lattice in figure 3(b), the dipole moment oscillated in the minimum period of one optical cycle of the driving field. Therefore, in accord with the analysis of the temporal profile of HHG in figure 2, the induced electron density in figure 3 explains the emergence of the pronounced even harmonics.

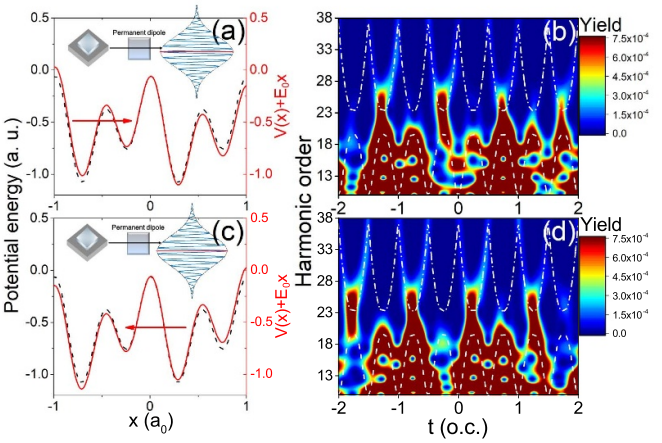

Figure 2. (a), (c) Schematic real-space representation of the field-free potential (black solid line) and field-dressed asymmetric periodic potentials (red dashed line). The peak of the laser field E_0 is represented by the magenta solid line in the center of the temporal profile of the laser field and is defined as the polarization direction. (b), (d) The temporal profile of the HHG spectra driven by the laser field with parallel (b) and anti-parallel (d) polarization directions. The white dashed line and white dash-dotted show the HHG trajectory predicted from the quasi-classical model for the interband transition from the conduction band CB1 to VB and CB2 to VB, respectively. The laser parameters used in the simulation are the same as those in figure 1.

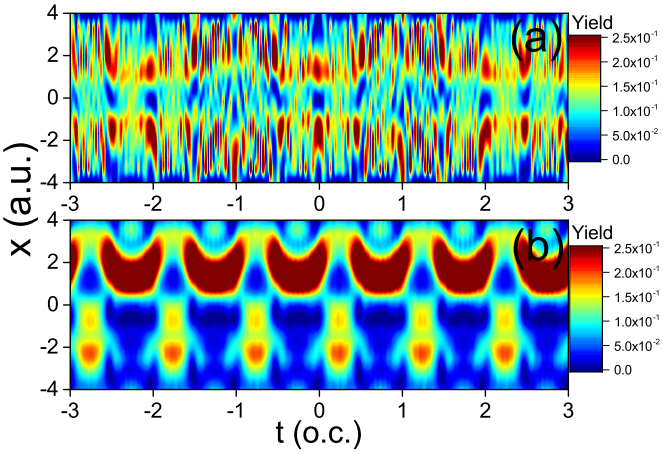

Figure 3. (a), (b) Evolution of the induced density of the valence band maximum state driven by the 24-cycle laser field. (a) Periodic symmetric potential; (b) periodic asymmetric potential. The laser parameters used in the simulation are the same as those in figure 1.

3.2. *Temporal profile of synthesized attosecond electric field*

As shown in figures 2(b) and (d), the temporal profile of HHG from periodic asymmetric potential has a minimum period of one optical cycle of the driving laser field. According to the analytical discussion in appendix B, the total dipole moment has the same formula as its counterpart generated in the consecutive optical cycle,

$$d(t)\mathrm{e}^{\mathrm{i}n\omega_0 t} = d(t+T_0)\mathrm{e}^{\mathrm{i}n\omega_0(t+T_0)} = d(t+T_0)\mathrm{e}^{\mathrm{i}n\omega_0(t)+\mathrm{i}2n\pi}. \tag{21}$$

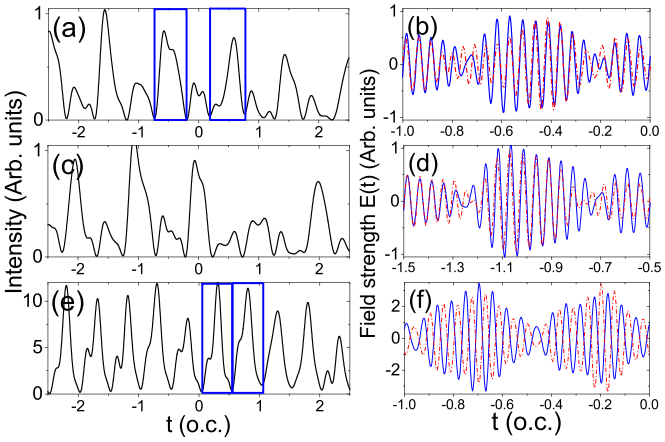

Figure 4. (a), (c), (e) Temporal profile of attosecond pulse trains (APT) synthesized from 10th to 20th harmonic from HHG spectra. (b), (d), (f) The electric field of the attosecond pulse and the electric field of the consecutive attosecond pulse are plotted by a blue solid line and a red dashed line, respectively. (a), (b) APT is synthesized from HHG spectra driven by a 24-cycle laser field from the periodic asymmetric potentials. (c), (d) The same as the top row but driven by the laser field with anti-parallel polarization. (e), (f) APT is synthesized from HHG spectra driven by a 24-cycle laser field from the periodic symmetric potentials. The laser parameters used in the simulation are the same as those in figure 1.

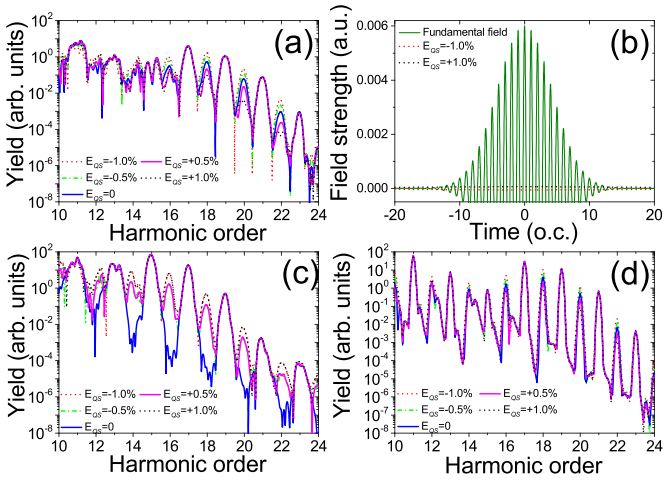

Figure 5. (a) HHG spectra for periodic asymmetric potential driven by the linear polarized 10-cycle laser field combined with a THz electric field with relative strength ratio $k_{\mathrm{THz}} = -1.0\%$, -0.5%, 0, $+0.5\%$ and $+1.0\%$, respectively. (b) The driving field used in (a). The 24-cycle laser field is plotted by a solid green line and the superimposed THz field with $k_{\mathrm{THz}} = 1.0\%$ and $k_{\mathrm{THz}} = -1.0\%$ are plotted by a black dashed-dotted line and red dashed line, respectively. Simulated laser parameters: for the fundamental pulse, a field strength $E_0 = 0.006$ a.u., FWHM $\tau = 10$-cycle, 1600 nm Gaussian laser field. For the control THz pulse, FWHM $\tau_2 = 267$ fs (15 o.c.), 102 400 nm pulse, the relative strength ratio $k_{\mathrm{THz}} = -1.0\%$, -0.5%, 0, $+0.5\%$ and $+1.0\%$, respectively. The dephasing time $T_2 = 1.0$ o.c. For the trapezoidal laser field used in figure 5(d), a 12-cycle 1600 nm laser field with 2 o.c. ramp-up.

Therefore, the attosecond pulse trains (APT) from the periodic asymmetric potential have the same CEP from pulse to pulse as shown in figures 4(b) and (d). Figure 4(a) shows the intensity profile of the APT from the periodic asymmetric potential. Figures 4(c) and (d) show the APT driven by the same laser field as the upper row except for the reversed laser polarization.

For comparison, the APT synthesized from the HHG of periodic symmetric potential is plotted in figures 4(e) and (f). Two attosecond bursts are generated in each optical cycle of the driving field. As shown in figure 4(f), the attosecond pulse has a π rad phase shift from pulse to pulse. Our result is in accordance with the result of the APT generated in the asymmetric molecule [27]. This indicates that, on the basis of HHG from periodic asymmetric potential, the APT with the same CEP could also be synthesized. APTs with the same CEP synthesized from HHG in periodic asymmetric lattices enable the control of ultrafast electron dynamics more accurately.

3.3. THz field modulated HHG in periodic asymmetric potentials

In this section, we investigate HHG in the periodic asymmetric potential driven by the multi-cycle field in the presence of a THz field. The HHG in the periodic asymmetric lattice driven by the multi-cycle laser in the presence of a weak static electric field [41, 42] was investigated [43, 44]. In this work, a THz electric field is employed as a control field since it is still difficult to obtain a static electric field with large field strength. The employed 1600 nm multi-cycle fundamental Gaussian pulse field is written as

$$E_1(t) = E_1 \exp\left[-4\ln(2)t^2/\tau_0^2\right]\cos(\omega_0 t). \tag{22}$$

The THz control field is written as,

$$E_{\mathrm{THz}}(t) = k_{\mathrm{THz}} E_1 \exp\left[-4\ln(2)(t)^2/\tau_2^2\right]\cos[\omega_{\mathrm{THz}} t]. \tag{23}$$

where a frequency of 2.928 THz is chosen for the THz electric field. The wavelength of the THz field is 64 times that of the fundamental 1600 nm driving field. The total field combined by the fundamental multi-cycle laser and THz field is given by,

$$E_{\mathrm{total}}(t) = E_1(t) + E_{\mathrm{THz}}(t), \tag{24}$$

where $E_1(t)$ and $E_{\mathrm{THz}}(t)$ are the temporal profiles of the multi-cycle fundamental field and THz field, respectively. k_{THz} is the relative strength ratio of the THz field with respect to the peak of the fundamental laser field.

Figure 5(a) shows the calculated HHG spectra in the periodic asymmetric potential driven by the multi-cycle pulse with a Gaussian envelope in the presence of the THz field. The 1600 nm fundamental laser field has a full-width-at-half maximum (FWHM) $\tau_p = 10$ o.c., and an amplitude $E_0 = 0.006$ a.u.

Figure 5(a) shows the HHG spectra for several magnitudes of the relative strength ratio varying from $k_{\mathrm{THz}} = -1.0\%$, -0.5%, 0.0%, $+0.5\%$, to $+1.0\%$. In the presence of a negative (positive) THz field, the yield of even harmonics increases (decreases). When k_{THz} varies from $k_{\mathrm{THz}} = +1.0\%$ to $k_{\mathrm{THz}} = -1.0\%$, the even harmonic increases with the variation of the relative strength ratio k_{THz}. Compared with the even harmonic, the yield of the odd harmonic is nearly invariant with respect to the superimposed THz field. Figure 5(b) shows the temporal waveform of the 1600 nm fundamental field and superimposed THz field with $k_{\mathrm{THz}} = -1.0\%$ and $k_{\mathrm{THz}} = +1.0\%$.

Figure 5(c) presents the HHG spectra in the periodic symmetric potential driven by a combined field composed of a multi-cycle laser field and THz control field. For the periodic symmetric potential, driven by a multi-cycle laser field, there are only odd harmonics. In the presence of a THz field, the temporal symmetry of the driving field will be broken. Thus, either the relative strength ratio k_{THz} is negative or positive, as the even harmonic is always enhanced with the increase in the magnitude of the relative strength ratio k_{THz} in the periodic symmetry potential.

The effect of the envelope on the driving field is also investigated in figure 5(d). The HHG is driven by the multi-cycle 1600 nm laser with a trapezoidal envelope in the presence of THz fields. The HHG spectra dependence on the relative strength ratio k_{THz} of the THz field is the same as compared with figure 5(a).

In figure 6, the left and right columns show the HHG from solids driven by the linear polarized 10-cycle, 1600 nm Gaussian laser field combined with a THz field with $k_{\mathrm{THz}} = -1.0\%$ and $k_{\mathrm{THz}} = +1.0\%$, respectively. Figures 6(a) and (b) show the recombination energy of the electrons and holes as a function of excitation time and recombination time obtained by the quasi-classical model and the excitation rates calculated by the Keldysh model.

Figures 6(c) and (d) show the temporal HHG emission by performing a wavelet Fourier transform of the total HHG current from the SBE calculation. The laser parameters in figures 6(c) and (d) are the same as the quasi-classical model analysis in the upper row.

For the periodic asymmetric potential, due to the parallel and anti-parallel directions between the permanent dipole and laser polarization directions, the excitation rate is strengthened in the former half cycle around $t = 0$ and reduced in the consecutive half cycle around $t = 0.5$ o.c., as shown by the temporal Keldysh excitation rates plotted by the green solid line in figures 6(a) and (b).

In figure 6(a), one may find that a positive THz field with a relative strength ratio $k_{\mathrm{THz}} = +1.0\%$ will increase the excitation rate in the 'weak' half-cycle around $t = 0.5$ o.c. At the same time, the excitation rate is decreased in the 'strong' half-cycle around $t = 0.0$ o.c. Therefore, the even harmonics are reduced on the HHG spectra in the presence of the THz field with $k_{\mathrm{THz}} = +1.0\%$. This is in accordance with the calculated temporal profile of HHG in figure 6(c).

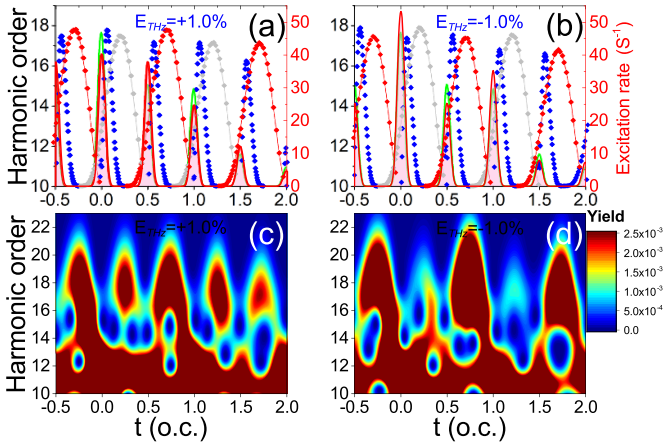

Figure 6. (a), (b) Harmonic order varies as a function of excitation time (blue scatters) and recombination time (gray and red scatters) calculated by classical saddle point method [19]. The gray (red) scatter indicates that the half-cycle harmonic emission is reduced (enhanced) due to the opposite (same) direction of permanent dipole and laser polarization directions. The excitation rate driven by the combined field of the fundamental laser pulse and THz field is plotted by a red-solid line. For comparison, the excitation rate driven by a single fundamental laser pulse is plotted by a solid green line. When the THz field is opposite (same) to the peak of the fundamental laser pulse, the strengthened (weakened) half cycle is enhanced (reduced) further due to the increase (decrease) of excitation rate caused by the THz electric field. (c), (d) Temporal profile of HHG driven by the combined field of the fundamental laser pulse and THz field. Left column: $k_{\mathrm{THz}} = +1.0\%$. Right column: $k_{\mathrm{THz}} = -1.0\%$. The laser parameters used in the simulation are the same as those in figure 5.

On the contrary, in figure 6(b), one may find that a negative THz field with a relative strength ratio $k_{\mathrm{THz}} = -1.0\%$ will make the excitation rate in the 'weak' half-cycle around $t = 0.5$ o.c. reduce further. At the same time, the excitation rate is enhanced in the 'strong' half-cycle around $t = 0.0$ o.c. Therefore, the even harmonics are enhanced in the HHG spectra in the presence of the THz field with $k_{\mathrm{THz}} = -1.0\%$. The temporal profile of the HHG in figure 6(d) further proves this.

In figures 5(a) and (d), the variation of the even harmonic with the relative strength ratio k_{THz} is more significant than the odd harmonic, which can be explained as follows. Driven by a combined field superimposed by the THz field, the excitation and harmonic radiation in the 'weak' half cycle can be reduced (enhanced) when $k_{\mathrm{THz}} = -1.0\%$ ($+1.0\%$). Let us suppose the yield of a given harmonic in the half optical cycle is equal to I_0. If the harmonic radiation is not suppressed in the 'weak' half cycle, then in each optical cycle, the total intensity of the odd harmonics can reach $2I_0$. On the contrary, if the harmonic radiation is completely suppressed in the 'weak' half cycle. Then, the total yield of the odd harmonic in each optical cycle is I_0. It can be considered approximately that the yield of odd harmonic varies in the range between I_0 and $2I_0$.

For even harmonics, the HHG radiation from the adjacent half cycles has completely destructive interference. For

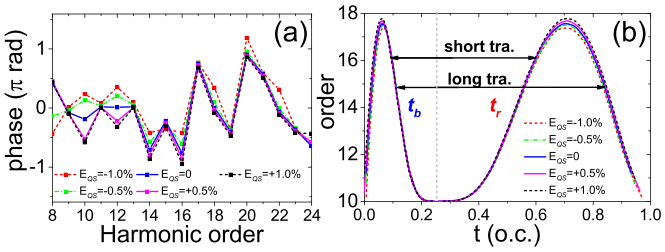

Figure 7. (a) The phase of the HHG spectra for periodic asymmetric potential driven by the combined field composed by the linear polarized 10-cycle Gaussian laser field and a THz field with relative strength ratio $k_{\mathrm{THz}} = -1.0\%$, -0.5%, 0, $+0.5\%$ and $+1.0\%$, respectively. (b) Harmonic order varies as a function of birth time t_{b} and recombination time t_{r} driven by the combined field. The laser parameters used in the simulation are the same as those in figure 5. For a given harmonic order, a monotonous variation of the birth time t_{b} and recombination time t_{r} of the carrier with the relative strength ratio k_{THz} is observed.

asymmetric systems, the harmonic radiation in the 'weak' half cycle can be reduced to nearly zero due to the opposite direction between the laser field and the permanent dipole moment. Then, the total yield of an even harmonic in each optical cycle has a yield of I_0. In the presence of a positive THz field, the intensity in the 'weak' half cycle has a similar intensity as the adjacent half optical cycle, and the total even order harmonics can be reduced to nearly zero. Thus, the total intensity of the even harmonic varies in the range of 0 to I_0. The yield of the even harmonic can vary by several orders of magnitude. Therefore, compared to the odd harmonic, the yield modulation of the even harmonic is more significant.

In figure 7, the superimposed THz field effect on the phases of HHG is investigated. As shown in figure 7(a), by varying the relative strength ratio k_{THz} from $+1\%$ to -1%, the phase of all harmonics in the plateau region increases. By shifting k_{THz} from $+1\%$ to -1%, even harmonic is enhanced, and the phase increases. As shown in figure 7(a), either the phases of the odd or even harmonics increase monotonously with k_{THz}. A linear shift of k_{THz} causes the monotonous variation of the amplitude of the combined driving field, while the amplitude of the driving field affects the propagation time of the electron–hole pair. Figure 7(b) shows the monotonous variation of the propagation time $\Delta t = (t_{\mathrm{r}} - t_{\mathrm{b}})$ of the carrier with the relative strength ratio k_{THz} predicted by the classical saddle-point method. The propagation time $\Delta t = (t_{\mathrm{r}} - t_{\mathrm{b}})$ modulated by the k_{THz} leads to the dependence of the phases of the harmonics on k_{THz}.

4. Conclusion

In this work, we investigated the HHG from the interaction between the MIR laser field and periodic asymmetric lattice. Even harmonic signals are observed in both the first and second plateaus in the HHG spectra driven by a multi-cycle pulse field. The phases of the odd harmonics shift π rad when the driving laser polarization direction is reversed, while the phase of the even harmonics has zero shift when the driving laser polarization direction is reversed. It is noted that the phase shifts by zero or π rad are not exactly satisfied in figure 1 for low-order harmonics. This is because the trajectories from the leading and tailing edges also contribute to the low-order harmonics, while the laser cycles in the leading and tailing edges do not have exactly the same amplitude.

Moreover, it is found that each pulse in the synthesized APT from HHG in a periodic asymmetric lattice shows the same CEP from pulse to pulse. APTs with the same CEP synthesized from HHG enable the control of ultrafast electron dynamics more accurately.

The effect of the THz field on the HHG from solids is investigated. The superimposed THz field can enhance or reduce even harmonics by modulating the excitation process in the consecutive half-optical cycles of the driving field. This indicates that the even harmonic yield and half-cycle HHG dynamics can be controlled by using k_{THz} as the control knob. In addition, by shifting the relative strength ratio k_{THz} of the superimposed terahertz field, the phase of the harmonic photons is varied monotonously.

Data availability statement

All data that support the findings of this study are included within the article (and any supplementary files).

Acknowledgments

This work was supported by the National Natural Science Foundation of China (No. 12104395), Zhejiang Provincial Natural Science Foundation of China (No. LQ22A040004), and the Ningbo Natural Science Foundation (Nos. 2021J153 and 2023J289).

Appendix A. Band structures and transition dipole moments

Figures 8(a) and (b) show the potential of the one-dimensional periodic symmetric and asymmetric potentials in this work, respectively. The band dispersion curves solved from the laser field free Schrödinger equation is shown in figure 8(c). Figure 8(d) shows the transition dipole moment (TDM) and phase of TDM in the reciprocal space computed from the Bloch-state basis expansion method.

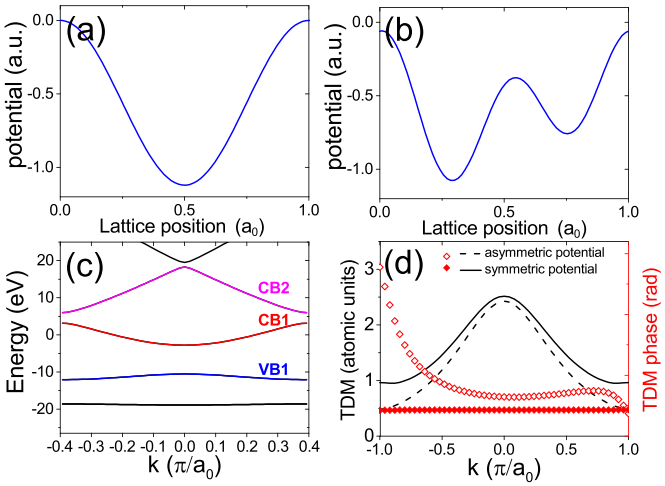

Figure 8. (a), (b) The potential of the one-dimensional periodic symmetric (a) and asymmetric (b) potentials. (c) The band structure for one-dimensional periodic asymmetric potentials. (d) The transition dipole moment (TDM) and the phase of TDM for one-dimensional periodic symmetric (a) and asymmetric (b) potentials.

Appendix B. The phases of the odd and even harmonics

For HHG current, a three-step scenario can be obtained from the semi-conductor Bloch equation model of Vampa *et al*'s work [18]. By using the Keldysh approximation, the interband current is expressed as follows [18],

$$j_{\mathrm{er}}(t)=\int_{\mathrm{BZ}}\mathrm{d}k d_x(k)\int_{-\infty}^{t}\mathrm{d}t_b F(t_b)d_x^*\left(\kappa_{t_b}\right)\mathrm{e}^{-\mathrm{i}S(k,t_b,t)}+\mathrm{c.c.}, \tag{25}$$

where $F(t)$ is the driving field, $d_x(k)$ is the transition dipole moment between the valence band and conduction band. $S(k,t_b,t)$ is the semi-classical action describing the propagation phase of the carrier born at t_b and recombine at t.

The Fourier component of the interband current is given by,

$$j_{\mathrm{er}}(\omega)=\int_{-\infty}^{\infty}\mathrm{d}t\mathrm{e}^{-\mathrm{i}\omega t}j_{\mathrm{er}}(t), \tag{26}$$

According to equations (25) and (26), the phase of the harmonic photons $\Phi_{\mathrm{intrinsic}}$ can be given by [45],

$$\Phi_{\mathrm{intrinsic}}=\omega t-S(k,t_b,t)=n\omega_0 t-S(k,t_b,t), \tag{27}$$

where ω_0 is the laser angular frequency, n is the harmonic order, t_b and t are the birth time and recombination time of the electron–hole pair, respectively. The total phase $\Phi_{\mathrm{intrinsic}}$ is contributed by the phase accumulated by the carrier $S(k,t_b,t)$, and phase $n\omega_0 t$ due to the time delay between the recombination time t and the reference time of the optical period of the driving field.

Since the HHG emission has a period of half optical cycle of the driving field, the interband current as shown in equation (25), can be rewritten as follows,

$$j_{\mathrm{er}}(t)=\sum_{n=0,1,2,\ldots n_f}d(t+nT_0/2), \tag{28}$$

where $d(t+nT_0)$ represents the interband current in a given half optical cycle, n denotes the nth half optical cycle in the temporal profile of the driving field.

The Fourier component of the interband current is then given by,

$$j_{\mathrm{er}}(\omega)=\int_{-\infty}^{\infty}\mathrm{d}t\sum_{n=0,1,2,\ldots n_f}d(t+nT_0/2)\mathrm{e}^{-\mathrm{i}\omega t}=\int_{-\infty}^{\infty}p_n(t)\mathrm{d}t, \tag{29}$$

where,

$$p_n(t)=\sum_{n=0,1,2,\ldots n_f}d(t+nT_0/2)\mathrm{e}^{\mathrm{i}n\omega_0(t+nT_0/2)}. \tag{30}$$

As shown in equation (29), by integrating $p_n(t)$ with time t, the total interband HHG spectra are obtained. By using a multi-cycle single-color laser, each optical cycle is nearly identical, thus we can focus on analyzing the HHG emission in one cycle. In each optical cycle,

$$p(t)=d(t)\mathrm{e}^{\mathrm{i}n\omega_0 t}+d(t+T_0/2)\mathrm{e}^{\mathrm{i}n\omega_0(t+T_0/2)}. \tag{31}$$

where $d(t)$ represents the radiation for the first half-cycle and $d(t+T_0/2)$ denotes the radiation for the following half-cycle. The radiation in the former half-cycle has the relation with its counterpart in the consecutive half-cycle as follows, $d(t)=-d(t+T_0/2)$.

Then the total oscillating dipole moment in each optical cycle can be expressed as follows,

$$p(t)=d(t)\mathrm{e}^{\mathrm{i}n\omega_0 t}\left[1-\mathrm{e}^{\mathrm{i}n\omega_0 T_0/2}\right]=d(t)\mathrm{e}^{\mathrm{i}n\omega_0 t}\left[1-\mathrm{e}^{\mathrm{i}n\pi}\right]. \tag{32}$$

Therefore, for even harmonic $n=2k(k\in 1,2,3,\ldots)$, $p(t)=0$, even harmonic disappear. For odd harmonic, $n=(2k-1)(k\in 1,2,3,\ldots)$, $p(t)=2d(t)\mathrm{e}^{\mathrm{i}n\omega_0 t}$, thus odd harmonic has constructive interference between the two adjacent half optical cycles and are strengthened.

For a periodic asymmetric lattice, the amplitudes of HHG from the former and the latter half-cycles are not equal, the amplitude of the weaker half-cycle is approximated as zero for simplifying discussions. Driven by a laser field that is parallel with respect to the permanent dipole moment, the total oscillating dipole moment generated in each optical cycle of the driving field is written as,

$$p(t)=d(t)\mathrm{e}^{\mathrm{i}n\omega_0 t}+0\times d(t+T_0/2)\mathrm{e}^{\mathrm{i}n\omega_0(t+T_0/2)}=d(t)\mathrm{e}^{\mathrm{i}n\omega_0 t}. \tag{33}$$

Therefore both the even and odd harmonics are preserved.

When periodic asymmetric potentials are driven by a laser field that has anti-parallel polarization with respect to the permanent dipole moment, the total oscillating dipole moment in each optical cycle can be expressed by,

$$p(t) = -d(t+T_0/2)\mathrm{e}^{\mathrm{i}n\omega_0(t+T_0/2)} = \begin{cases} +d(t)\mathrm{e}^{\mathrm{i}n\omega_0 t}, n = \text{even} \\ -d(t)\mathrm{e}^{\mathrm{i}n\omega_0 t}, n = \text{odd} \end{cases}. \tag{34}$$

Compare equations (33) and (34) in the above analytical discussion, when the laser polarization direction of the multi-cycle pulse is reversed, the temporal profile of even harmonic has the same formula. This indicates the phase of even harmonic is the same and is independent of laser polarization. In contrast, for odd harmonics, when the direction of laser polarization is reversed, there is a π rad phase shift.

For an inverse symmetric system, when the direction of laser polarization is reversed, the total oscillating dipole moment is written as,

$$p(t) = -d(t)\mathrm{e}^{\mathrm{i}n\omega_0 t}\left[1 - \mathrm{e}^{\mathrm{i}n\pi}\right] \tag{35}$$

Compare equation (32) with equation (35), the odd harmonic from periodic symmetric potential, should have π rad phase shift when the laser polarization direction is reversed. The reverse of the polarization direction of the field is equivalent to the phase shift by a half period in a multi-cycle pulse. Therefore, for any system, the odd harmonics change by π rad when the electric field is reversed.

ORCID iDs

Tian-Jiao Shao https://orcid.org/0000-0001-5178-4544
Qiu-Lan Zhang https://orcid.org/0000-0002-3153-3577

References

[1] Dubietis A, Jonušauskas G and Piskarskas A 1992 *Opt. Commun.* **88** 437–40
[2] Ishii N, Kaneshima K, Kitano K, Kanai T, Watanabe S and Itatani J 2014 *Nat. Commun.* **5** 3331
[3] Vampa G, Hammond T J, Thiré N, Schmidt B E, Légaré F, McDonald C R, Brabec T, Klug D D and Corkum P B 2015 *Phys. Rev. Lett.* **115** 193603
[4] Ndabashimiye G, Ghimire S, Wu M, Browne D A, Schafer K J, Gaarde M B and Reis D A 2016 *Nature* **534** 520–3
[5] You Y S *et al* 2017 *Opt. Lett.* **42** 1816–9
[6] Yoshikawa N, Tamaya T and Tanaka K 2017 *Science* **356** 736–8
[7] Tancogne-Dejean N, Mücke O D, Kärtner F X and Rubio A 2017 *Nat. Commun.* **8** 745
[8] Jia G R, Huang X H and Bian X B 2017 *Opt. Express* **25** 23654–62
[9] You Y S, Reis D A and Ghimire S 2017 *Nat. Phys.* **13** 345–9
[10] Wang X Q and Bian X B 2021 *Phys. Rev.* A **103** 053106
[11] Mrudul M, Tancogne-Dejean N, Rubio A and Dixit G 2020 *npj Comput. Mater.* **6** 1–9
[12] Lakhotia H, Kim H, Zhan M, Hu S, Meng S and Goulielmakis E 2020 *Nature* **583** 55–59
[13] Mrudul M S, Álvaro J-G, Ivanov M and Dixit G 2021 *Optica* **8** 422–7
[14] Liu J Q and Bian X B 2021 *Phys. Rev. Lett.* **127** 213901
[15] Zhao Y T, Ma S, Jiang S C, Yang Y J, Zhao X and Chen J G 2019 *Opt. Express* **27** 34392–404
[16] Wu D, Li L, Zhan Y, Huang T, Cui H, Li J, Lan P and Lu P 2022 *Phys. Rev.* A **105** 063101
[17] Qiao Y, Huo Y Q, Jiang S C, Yang Y J and Chen J G 2022 *Opt. Express* **30** 9971–82
[18] Vampa G, McDonald C R, Orlando G, Klug D D, Corkum P B and Brabec T 2014 *Phys. Rev. Lett.* **113** 073901
[19] Vampa G, McDonald C R, Orlando G, Corkum P B and Brabec T 2015 *Phys. Rev.* B **91** 064302
[20] Du T Y and Bian X B 2017 *Opt. Express* **25** 151–8
[21] Li L, Lan P, Zhu X, Huang T, Zhang Q, Lein M and Lu P 2019 *Phys. Rev. Lett.* **122** 193901
[22] Liu X, Zhu X, Li L, Li Y, Zhang Q, Lan P and Lu P 2016 *Phys. Rev.* A **94** 033410
[23] Saito N, Xia P, Lu F, Kanai T, Itatani J and Ishii N 2017 *Optica* **4** 1333–6
[24] Jiang S, Chen J, Wei H, Yu C, Lu R and Lin C D 2018 *Phys. Rev. Lett.* **120** 253201
[25] Chen Z Y and Qin R 2019 *Opt. Express* **27** 3761–70
[26] Neufeld O, Podolsky D and Cohen O 2019 *Nat. Commun.* **10** 405
[27] Lan P, Lu P, Cao W, Li Y and Wang X 2007 *Phys. Rev.* A **76** 021801
[28] Frumker E *et al* 2012 *Phys. Rev. Lett.* **109** 233904
[29] Akagi H, Otobe T, Staudte A, Shiner A, Turner F, Dörner R, Villeneuve D and Corkum P 2009 *Science* **325** 1364–7
[30] Bian X B and Bandrauk A D 2010 *Phys. Rev. Lett.* **105** 093903
[31] Chen J, Yu S, Li Y, Wang S and Chen Y 2017 *Chin. Phys.* B **26** 094209
[32] Feit M D, Fleck J A and Steiger A 1982 *J. Comput. Phys.* **47** 412–33
[33] Wu M, Ghimire S, Reis D A, Schafer K J and Gaarde M B 2015 *Phys. Rev.* A **91** 043839
[34] Guan Z, Zhou X X and Bian X B 2016 *Phys. Rev.* A **93** 033852
[35] Huang T, Zhu X, Li L, Liu X, Lan P and Lu P 2017 *Phys. Rev.* A **96** 043425
[36] Liu L, Zhao J, Dong W, Liu J, Huang Y and Zhao Z 2017 *Phys. Rev.* A **96** 053403
[37] Mrudul M S, Pattanayak A, Ivanov M and Dixit G 2019 *Phys. Rev.* A **100** 043420
[38] Meier T, vol Plessen G, Thomas P and Koch S W 1994 *Phys. Rev. Lett.* **73** 2638
[39] Li J, Zhang X, Fu S, Feng Y, Hu B and Du H 2019 *Phys. Rev.* A **100** 043404
[40] Itatani J, Levesque J, Zeidler D, Niikura H, Pépin H, Kieffer J C, Corkum P B and Villeneuve D M 2004 *Nature* **432** 867–71
[41] Bao M Q and Starace A F 1996 *Phys. Rev.* A **53** R3723–6
[42] Hong W, Lu P, Cao W, Lan P and Wang X 2007 *J. Phys. B: At. Mol. Opt. Phys.* **40** 2321
[43] Silaev A, Romanov A and Vvedenskii N 2022 High harmonicgeneration from oriented asymmetric molecules in the presence of static electric field *J. Phys.: Conf. Ser.* **2249** 012004
[44] Fan J G, Li X Y, Jia X F and Miao X Y 2022 *Chem. Phys. Lett.* **787** 139201
[45] Balcou P, Salières P, L'Huillier A and Lewenstein M 1997 *Phys. Rev.* A **55** 3204–10

eb of Science™ Core Collection

经检索《Web of Science™ Core Collection》，下述论文被《SCI - Expanded》收录。（数据获取：2023年08月10日）

标题:Control of high-harmonic generation from periodic asymmetric lattices

作者:Shao, TJ(Shao, Tianjiao) Zhang, QL(Zhang, Qiulan) Song, YD(Song, Yadong) Zou, HQ(Zou, Huanqing)

来源出版物:JOURNAL OF PHYSICS B-ATOMIC MOLECULAR AND OPTICAL PHYSICS **卷**:56 **期**:16 **文献号**:165401

出版时间:2023,AUG 28 **DOI**:10.1088/1361-6455/ace507

出版商:IOP Publishing Ltd **出版商地址**:TEMPLE CIRCUS, TEMPLE WAY, BRISTOL BS1 6BE, ENGLAND

文献类型:Article **语种**:English

入藏号:WOS:001037788300001 **IDS号**:N5ZK1

地址:[Shao, Tian-Jiao; Zhang, Qiu-Lan; Zou, Huan-Qing] NingboTech Univ, Sch Informat Sci & Engn, Ningbo 315100, Peoples R China; [Shao, Tian-Jiao; Song, Ya-Dong] Chinese Acad Sci, Wuhan Inst Phys & Math, Innovat Acad Precis Measurement Sci & Technol, State Key Lab Magnet Resonance & Atom & Mol Phys, Wuhan 430071, Peoples R China; [Song, Ya-Dong] Zhejiang Ocean Univ, Sch Math Phys & Informat Sci, Zhejiang 316022, Peoples R China

通讯作者:Shao, TJ (通讯作者)，NingboTech Univ, Sch Informat Sci & Engn, Ningbo 315100, Peoples R China.; Shao, TJ; Song, YD (通讯作者)，Chinese Acad Sci, Wuhan Inst Phys & Math, Innovat Acad Precis Measurement Sci & Technol, State Key Lab Magnet Resonance & Atom & Mol Phys, Wuhan 430071, Peoples R China.; Song, YD (通讯作者)，Zhejiang Ocean Univ, Sch Math Phys & Informat Sci, Zhejiang 316022, Peoples R China.

电子邮件:shaotj@nit.zju.edu.cn; yadong_s@163.com

ISSN:0953-4075 **电子ISSN**:1361-6455

ISO 来源文献缩写:J. Phys. B-At. Mol. Opt. Phys. **来源出版物页码计数**:10

注：

以上检索结果均得到被检索人的确认。本证明编号：NBT-SCIE-2023-6050

《SCI - Expanded》检索结果（收录情况）

浙大宁波理工学院图书馆

检索人(签名)：

审核人(签章)：

浙江大学宁波理工学院 图书馆 检索证明专用章

2023年08月21日

...tes™ Journal Citation Reports®

经检索《Web of Science™》的JCR数据库，期刊《JOURNAL OF PHYSICS B-ATOMIC MOLECULAR AND OPTICAL PHYSICS》2022年JCR的影响因子情况：

ISSN：0953-4075

eISSN：1361-6455

2022年影响因子：1.6

OPTICS：Q4

PHYSICS, ATOMIC, MOLECULAR & CHEMICAL：Q4

注：

1.以上检索结果均得到被检索人的确认。证明编号：NBT-SCIE-2023-6050-IF2022

2.论文的期刊影响因子应与该论文所发表期刊的年份相对应。

3.因JCR的最新数据截至到2022年，2023年出版论文的期刊影响因子以2022年的期刊影响因子为参考。

《JOURNAL CITATION REPORTS（JCR）》检索结果

浙大宁波理工学院图书馆

检索人(签名)：

审核人(签章)：

检索证明专用章

2023年08月21日